Surface & Coatings Technology 426 (2021) 127803

Contents lists available at ScienceDirect

Surface & Coatings Technology

journal homepage: www.elsevier.com/locate/surfcoat

Investigation of iridium, ruthenium, rhodium, and palladium binary metal oxide solid solution thin films for implantable neural interfacing applications

Gregory Taylor [a,*], Jeffrey Shallenberger [b], Saxon Tint [c], Andrew Fones [d], Hugh Hamilton [d], Lei Yu [e], Shahram Amini [f], Jeffrey Hettinger [a]

[a] Department of Physics and Astronomy, Rowan University, Glassboro, NJ 08028, USA
[b] Materials Characterization Lab, Pennsylvania State University, University Park, PA 16802, USA
[c] Johnson Matthey Inc., Manufacturing Centre, San Diego, CA 92128, USA
[d] Johnson Matthey Technology Centre, Sonning Common, Reading RG4 9NH, UK
[e] Department of Chemistry and Biochemistry, Rowan University, Glassboro, NJ 08028, USA
[f] Johnson Matthey Inc., Center for Coatings and Surface Solutions, Medical Components, West Chester, PA 19380, USA

ARTICLE INFO

Keywords:
Combinatorial synthesis
Reactive magnetron sputtering
Solid solutions
Platinum group metal oxides
Neurostimulation electrodes

ABSTRACT

Metal oxide solid solution thin films containing binary mixtures of iridium, ruthenium, rhodium, and palladium were combinatorially synthesized by DC reactive magnetron sputtering to investigate the compositional dependence of properties relevant to neural interfacing applications. The binary metal oxides studied included $Ir_{(1-x)}M_xO_y$ where M = Pd, Rh, and Ru. The properties of the binary metal oxides are compared to that of their single metal oxide endmembers which include palladium oxide (PdO_x), ruthenium oxide (RuO_x), rhodium oxide (RhO_x), and iridium oxide (IrO_x). The binary metal oxides exceed the electrochemical performance of their respective single metal oxide endmembers (as measured by cyclic voltammetry) at film thicknesses generally greater than 700 nm. The binary metal oxide concentrations which produce robust microstructures and exceptional electrochemical performance have been identified to be but are not limited to $x \geq 0.5$ for $Ir_{(1-x)}Rh_xO_y$, $x \geq 0.34$ for $Ir_{(1-x)}Ru_xO_y$, and $x \geq 0.14$ for $Ir_{(1-x)}Pd_x O_y$. XPS analyses suggest that the electrochemical enhancements observed are at least partly due to the presence of higher oxidation states in the binary metal oxides when compared to that of the corresponding single metal oxide endmembers.

1. Introduction

Treatment of many neurological diseases and disorders is traditionally achieved through use of pharmaceuticals or surgical procedures. The former is appealing due to the diverse number of drugs that are available for the treatment of a wide range of conditions, the relative ease of intake by the patient, and the relative ease of production. However, pharmaceuticals lack specificity in their treatment and can become less effective over time due to the development of drug tolerance [1–3]. Surgical approaches, while necessary in some circumstances, can often be traumatic and come with a greater risk of infection [4–6]. Moreover, surgical procedures often require use of pharmaceuticals to assist in the recovery process.

Implantable neural interfacing devices supplant many traditional pharmaceutical and surgical treatments due to their high specificity and efficacy while minimizing or eliminating many of the peripheral and downstream effects associated with use of pharmaceuticals [7–11]. These devices often require only minimally invasive implantation resulting in shorter recovery times and reduced risk of infection. Furthermore, because of the mechanism leading to their effectiveness, negative side-effects such as dependence or treatment tolerance are not present, thus granting extended efficacy *via* long-term implantation [12–16]. The trajectory for further refinement of neural interfacing devices is in large part predicated on increased miniaturization of devices and electrodes which enable higher spatial resolution, precision, and reliability [17–21].

An important characteristic of sputtered IrO_x and Ir-containing binary and ternary metal oxide systems is the growth of nanoflake

* Corresponding author.
E-mail address: taylor6q@students.rowan.edu (G. Taylor).

https://doi.org/10.1016/j.surfcoat.2021.127803
Received 15 July 2021; Received in revised form 24 September 2021; Accepted 7 October 2021
Available online 15 October 2021

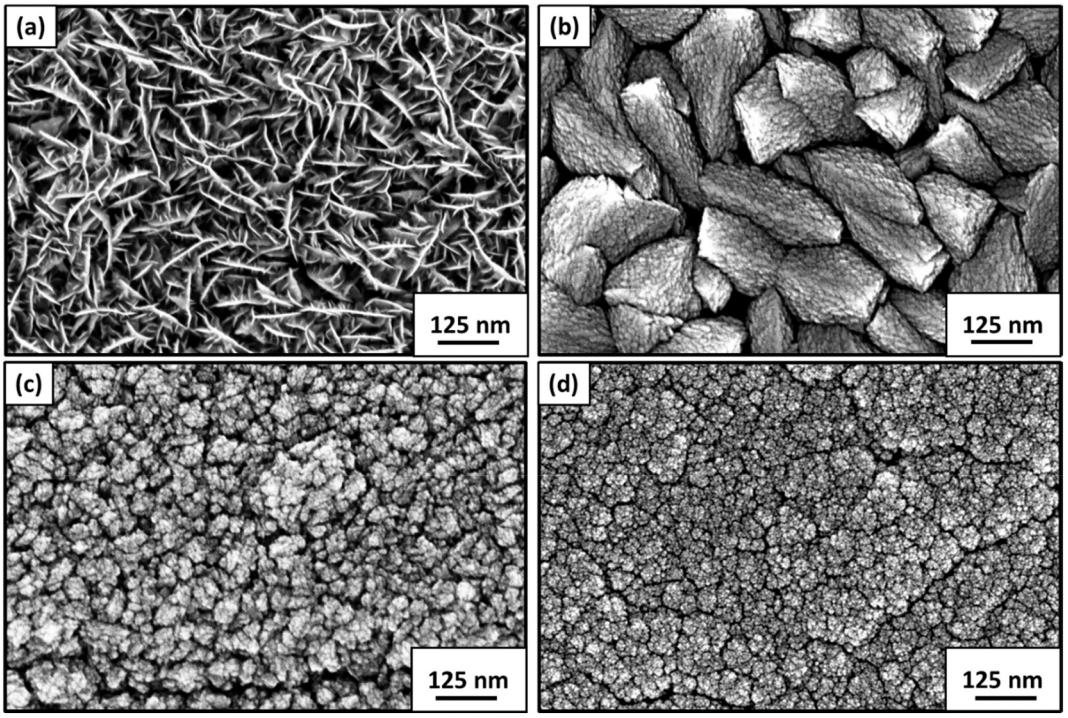

Fig. 1. SEM micrographs of the surface microstructure of (a) IrO_x, (b) PdO, (c) RuO_x, and (d) Rh_xO_y thin films synthesized at 20% OPP and 30 mTorr WP.

microstructure [22–24] as shown in Fig. 1a. This microstructure has been observed to increase the charge exchange properties of films due to its high surface area [25,26]. However, despite this electrochemical enhancement, nanoflake microstructure has been reported to be mechanically fragile [26]. Thus, there is a need to identify and develop new materials for implantable neural interfacing applications to enhance charge exchange between the electrode-tissue interface, in the absence of non-nanoflake microstructure. This work addresses this need by investigating the changes in microstructure, chemical composition and state, and cathodic charge storage capacity (CSC_C) performance (as a function of thickness) in $Ir_{(1-x)}M_x$ binary metal oxide films where M = Pd, Rh, Ru.

2. Materials and methods

$Ir_{(1-x)}M_xO_y$ (M = Pd, Rh, Ru) depositions were performed using DC reactive magnetron sputtering with a TM-Vacuum Smart-Jar (U.S.A.) system. Sputtering was performed with three two-inch circular planar cathodes (Angstrom Sciences ONYX cathode, U.S.A.). The two-inch Ir, Ru, Rh, and Pd targets were of 99.95% Purity (Johnson Matthey Inc., U.K.). The Ru and Rh targets had thicknesses of 0.64 cm, and the Ir and Pd targets had thicknesses of 0.32 cm. Targets were indirectly cooled with flowing water at 14 °C.

Depositions were performed at ambient substrate temperature with a working distance of 10 cm. Single metal oxides were sputtered from a single cathode and were supplied 100 W of power from a pulsed DC power supply (Advanced Energy Pinnacle Plus, U.S.A.). Two Ir targets were supplied 25 W of power each from two different pulsed DC power supplies operated at a frequency of 140 kHz and a reverse period of 1.8 μs (Advanced Energy Pinnacle Plus, U.S.A., and Trumpf Hüttinger TruPlasma DC1000, DE). The Pd, Rh & Ru targets were supplied 50 W of power from a DC power supply (Advanced Energy MDX-1000, U.S.A.).

Two nominally identical depositions were performed. The first films were deposited onto 316 stainless steel foil (316 SS) (McMaster-Carr, U.S.A.) while the secondary films were deposited on SiO_2/Si substrates (University Wafer, U.S.A.). Depositions were performed at 30 mTorr working pressure (WP) and 20% oxygen partial pressure (OPP), with an overall gas flow rate of 50 sccm (O_2 + Ar). Prior to deposition, substrates were RF etched for a duration of 5 min at 100 W with high purity Ar gas flowing at 50 sccm at a working pressure of 20 mTorr to insure excellent adhesion.

The cathodic charge storage capacity (CSC_C) was measured with a potentiostat/galvanostat (Metrohm Autolab, PGSTAT204, NL). A three-electrode setup was utilized (ALS-CO Ltd. Plate Material Evaluating Cell, JP) using Ag|AgCl reference electrode (RE) (ALS-Co Ltd. RE-1B, JP), a coiled platinum wire counter electrode (CE), and the coated 316 SS served as the working electrode (WE). The geometric surface area of the WE in the cell was 0.46 cm^2. The electrolyte used was a phosphate-buffered saline (PBS) solution (VWR Ultra-Pure PBS, 10×, USP sterile, U.S.A.) diluted to 0.1 M with DI water and had a pH of 7.4. The voltage was swept at 0.10 V/s over the −0.4–1.0 V voltage window for 5 cycles, with the CSC_C values calculated from the 5th cycle voltammograms. Only the CSC_C of the binary metal oxide films which possessed similar metallic concentrations within a compositional tolerance of x ± 0.01 (based on relative metallic concentration) and which possessed different thicknesses from the combinatorial matrix are reported.

Surface morphology of the as-deposited films on 316 SS substrates was examined with a field emission SEM (Thermo-Fisher Scientific APREO-S, U.S.A.). Elemental composition of the films deposited on 316 SS substrates was evaluated using energy dispersive spectroscopy (EDS) (Oxford Instruments Ultim Max, U.K.) and is presented as the ratio of metals measured in the films. Film thicknesses were measured using stylus profilometry (Ambios XP-2 Surface Profiler, U.K.) using a liftoff method on films deposited on SiO_2/Si substrates from the secondary deposition. Using JMP® software, a standard least squares model was used to estimate film thicknesses that were not measured directly on the witness sample.

To identify key relationships between parameters, a full factorial design was selected that took into consideration the ratio of metals, oxygen content (at. %), and the thickness dependent CSC_C of the single and binary metal oxides.

XPS experiments were performed using a Physical Electronics VersaProbe III instrument equipped with a monochromatic Al-Kα x-ray source (hν = 1486.6 eV) and a concentric hemispherical analyzer.

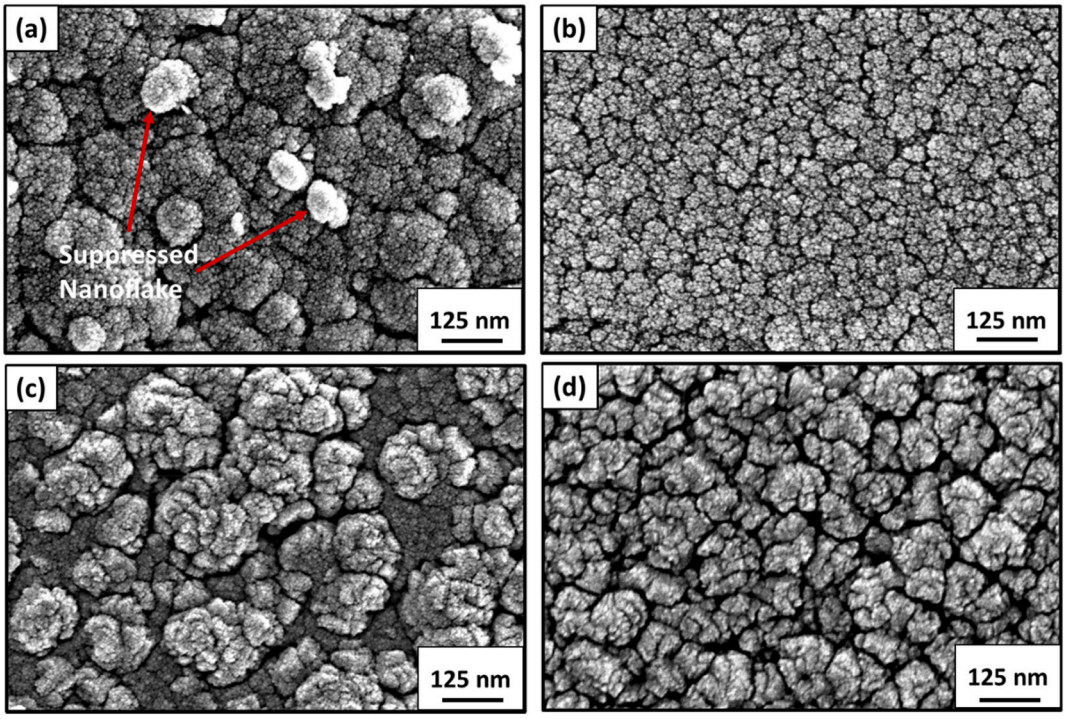

Fig. 2. SEM micrographs of $Ir_{(1-x)}Pd_xO_y$ films deposited on 316 SS substrates with Pd content of, (a) x = 0.14, (b) x = 0.50, (c) x = 0.90, and (d) x = 0.95.

Table 1
Microstructures based on M-content for $Ir_{(1-x)}M_xO_y$ metal oxide systems.[a]

Oxide system	Nanoflake	Intermediate	M_x
$Ir_{(1-x)}Pd_xO_y$	$x < 0.14$	$0.14 \leq x \leq 0.90$	$x > 0.90$
$Ir_{(1-x)}Ru_xO_y$	$x < 0.34$	$0.34 \leq x \leq 0.70$	$x > 0.70$
$Ir_{(1-x)}Rh_xO_y$	$x < 0.50$	$x \geq 0.50$	$x \geq 0.50$

[a] Films synthesized at 20% OPP and 30 mTorr WP.

Charge neutralization was performed using both low energy electrons (<5 eV) and argon ions. The binding energy (BE) axis was calibrated using sputter cleaned Cu ($Cu\ 2p_{3/2} = 932.62$ eV, $Cu\ 3p_{3/2} = 75.1$ eV) and Au foils ($Au\ 4f_{7/2} = 83.96$ eV). Peaks were charge referenced to the CH_x band in the carbon 1 s spectra at 284.8 eV. Measurements were made at a takeoff angle of 45° with respect to the sample surface plane. This resulted in a typical sampling depth of 3–6 nm (95% of the signal originated from this depth or shallower).

3. Results

3.1. Microstructure

Representative microstructures of $Ir_{(1-x)}Pd_xO_y$ films are presented in Fig. 2a–d. $Ir_{(1-x)}Pd_xO_y$ films with low Pd content (x = 0.14) develop nano-spherical grains that cluster into large irregular shapes as shown in Fig. 2a. At these high Ir concentrations some evidence of nanoflake microstructure is present as indicated in Fig. 2a. However, incorporation of even small amounts of Pd is largely able to suppress the development of the nanoflake microstructure. In the intermediary solid solution region (0.14 < x < 0.90), the microstructure is dominated by nano-spherical grains that combine into small clusters as shown in Fig. 2b. On the opposite end of the compositional gradient where Pd concentrations are considerably higher (x ≥ 0.90), $Ir_{(1-x)}Pd_xO_y$ films adopt microstructure that begins to resemble that of the PdO_x (Fig. 2b) end-member as shown in Fig. 2c and d, for x = 0.90 and 0.95, respectively. The microstructure in films with x > 0.90 is uniquely characterized by large irregularly-shaped polygonal grains that grow alongside the nano-

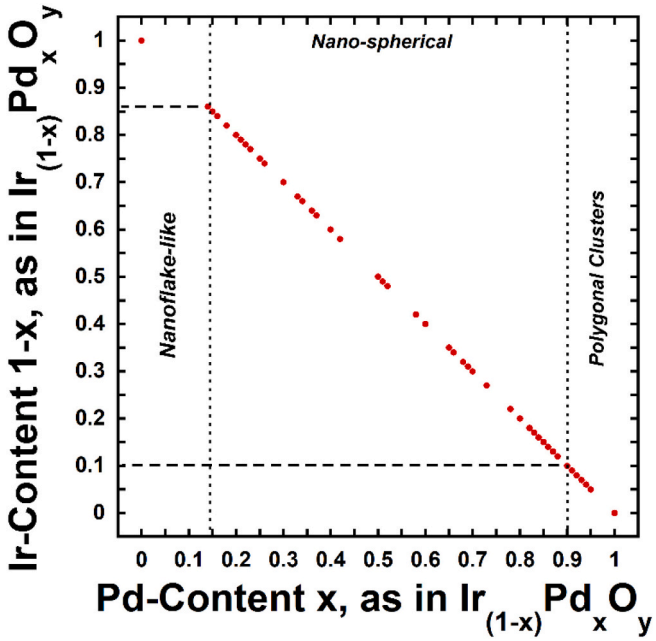

Fig. 3. Composition of $Ir_{(1-x)}Pd_xO_y$ based on relative metallic content and corresponding expected microstructural characteristics.

spherical grains observed in the intermediate solid solution region (0.14 < x < 0.90). An overview of the compositional ranges investigated based on metallic content and expected microstructural characteristics are presented in Table 1 and Fig. 3.

This microstructural evolution is notable as it suggests that, initially, Pd is substitutionally replaced by Ir in PdO_x at Pd metal sites at high Pd concentrations (x ≥ 0.90). These microstructural characteristics indicate the primary solubility limits of Ir into PdO_x. At decreasing x, this is followed by a region that can be characterized as the intermediate solid

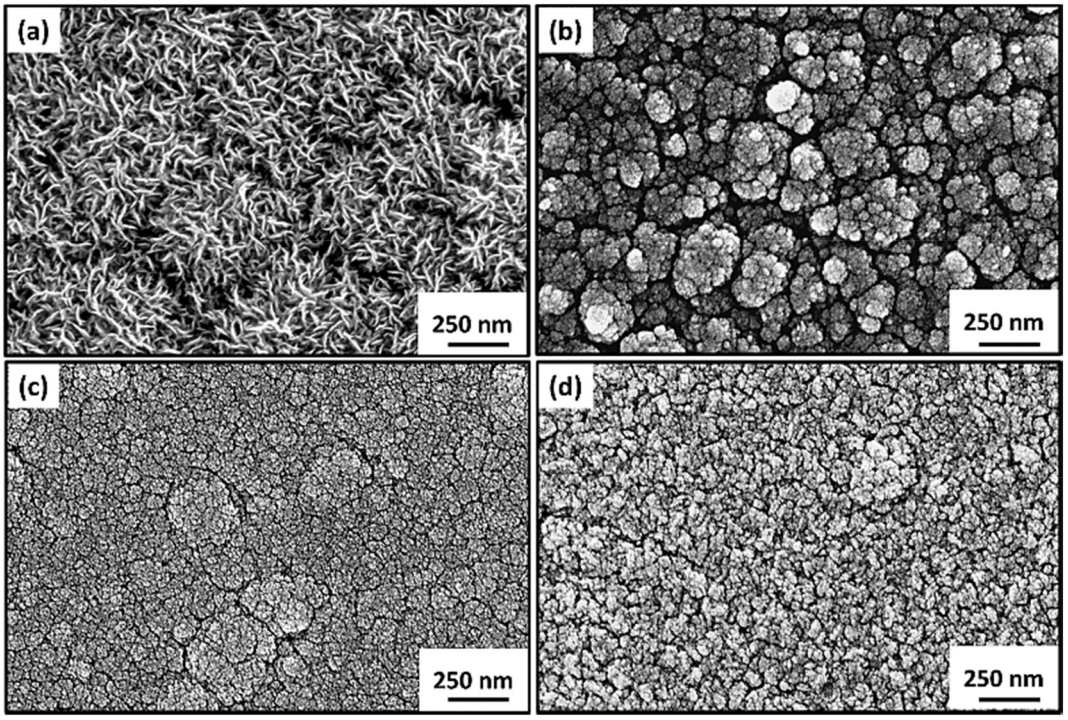

Fig. 4. SEM micrographs of $Ir_{(1-x)}Ru_xO_y$ deposited on 316 SS substrates with Ru content of (a) x = 0.10 (b) x = 0.24 (c) x = 50, and (d) x = 0.70.

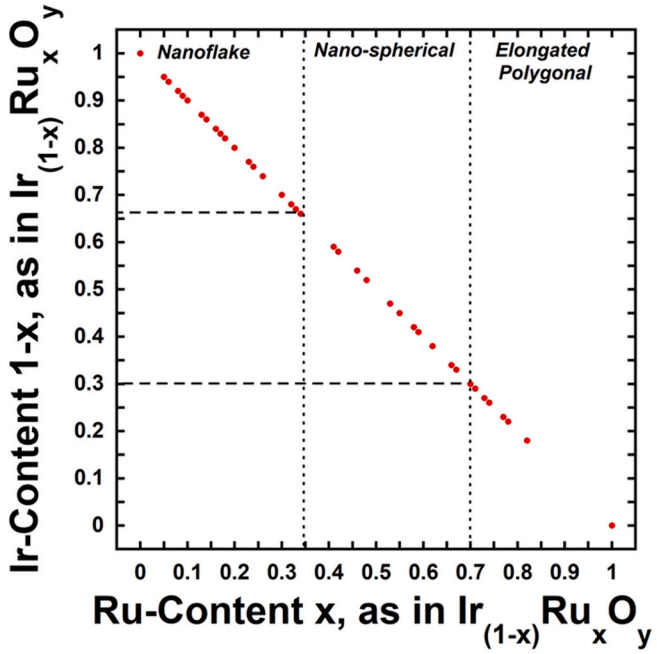

Fig. 5. Composition of $Ir_{(1-x)}Ru_xO_y$ based on relative metallic content and corresponding expected microstructural characteristics.

solution ($0.14 < x < 0.90$) for the $Ir_{(1-x)}Pd_xO_y$ system. The crystal structure over this intermediate region is disordered and deviates from the structure of either of the single metal oxide endmembers, *i.e.* PdO_x and IrO_x. Finally, at Pd concentrations of approximately $x \leq 0.14$, films are in a primary solid solution zone as indicated by the presence of nanoflake-like microstructure. Within this compositional region, however, the IrO_x crystal structure is primary with Pd substituting into the Ir-lattice sites.

Representative microstructures of $Ir_{(1-x)}Ru_xO_y$ films over a range of compositions are shown in Fig. 4a–d. Nanoflake and nanoflake-like microstructures (Fig. 4a) develop in $Ir_{(1-x)}Ru_xO_y$ films below approximately $x < 0.34$. As the Ru content (x) approaches 0.34, the microstructure of $Ir_{(1-x)}Ru_xO_y$ consisted of large approximately spherical clusters of nanospherical grains as shown in Fig. 4b. Mirroring the $Ir_{(1-x)}Pd_xO_y$ system, the $Ir_{(1-x)}Ru_xO_y$ similarly develops nanospherical grains in the intermediary compositional solid solution range ($0.34 > x > 0.7$) as depicted in Fig. 4c. As shown in Fig. 4d, for high Ru concentrations ($x \geq 0.70$) the $Ir_{(1-x)}Ru_xO_y$ grains remain nano-spherical in size but cluster into irregular polygonal shapes reminiscent of the RuO_x endmember oxide shown in Fig. 1c. The range of compositions based on the atomic ratio of Ir/Ru and the corresponding distinguishing microstructural characteristics are summarized in Table 1 and Fig. 5.

Microstructures of films which form at various compositions of $Ir_{(1-x)}Rh_xO_y$ are presented in Fig. 6a–d. At concentrations of $x < 0.50$, the $Ir_{(1-x)}Rh_xO_y$ films develop nanoflakes similar to those shown in Fig. 1a and mixed nano-spherical/flake microstructure as shown in Fig. 6a. $Ir_{(1-x)}Rh_xO_y$ with Rh concentrations of approximately $x \approx 0.50$ grow variably-sized tightly-packed clusters of nano-spherical grains as shown in Fig. 6b. At $x > 0.50$ (Fig. 6c–d), films grow clusters of nano-spherical grains. Additionally, the complete suppression of nanoflake growth was observed to be at Rh concentrations of $x \geq 0.50$. No clear microstructural distinction can be made between the intermediate compositions ($x > 0.50$, Fig. 6c) and high Rh content films ($x > 0.85$, Fig. 6d). This lack of distinction in microstructure extends to the microstructure of the RhO_x (Fig. 1d) endmember. This characteristic may suggest that Ir is equally soluble into RhO_x as Rh is into IrO_x. The range of compositions based on the ratio of metals and expected microstructures are summarized in Table 1 and Fig. 7.

3.2. Chemical analysis

3.2.1. EDS

The chemical composition as measured by EDS for each of the binary metal oxides in which XPS was performed are presented in Tables 2, 3, and 4 for $Ir_{(1-x)}Pd_xO_y$, $Ir_{(1-x)}Ru_xO_y$, and $Ir_{(1-x)}Rh_xO_y$, respectively. The quantification of chemical composition using EDS rather than XPS was

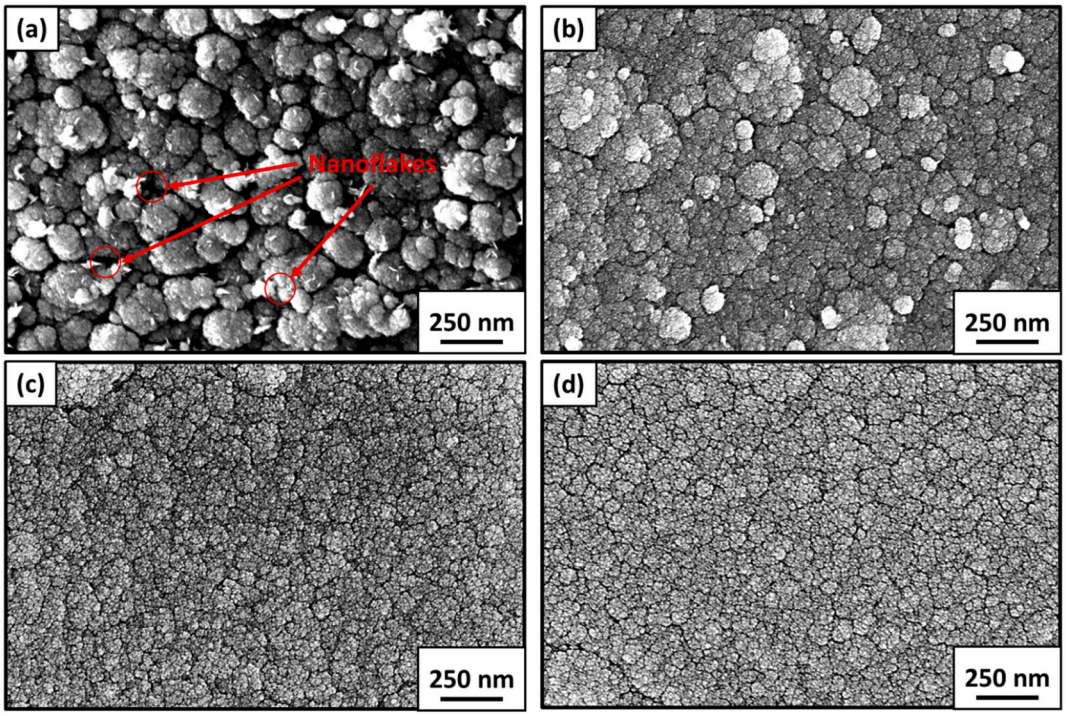

Fig. 6. SEM micrographs of $Ir_{(1-x)}Rh_xO_y$ deposited on 316 SS substrates synthesized at 30 mTorr and 20% OPP with Rh content of, (a) x = 0.42, (b) x = 0.50, (c) x = 0.80, and, (d) x = 0.85.

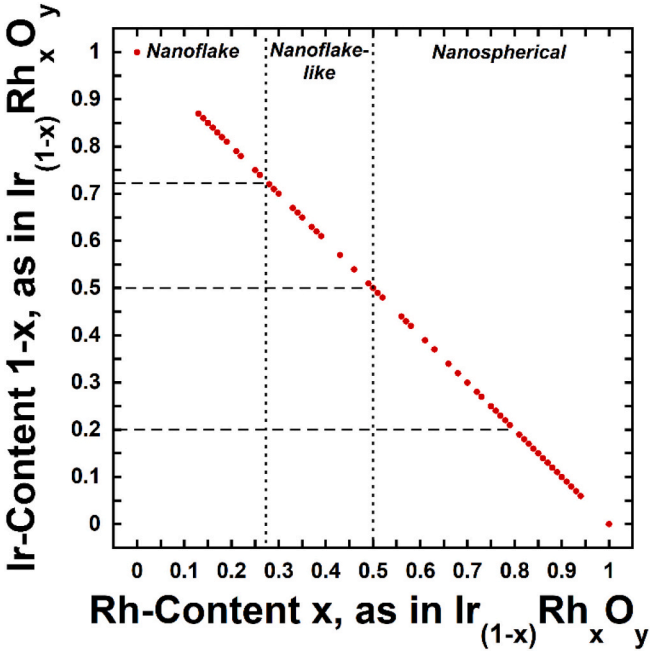

Fig. 7. Composition of $Ir_{(1-x)}Rh_xO_y$ based on relative metallic content and corresponding expected microstructural characteristics.

selected due to severe interference in XPS spectral lines which differ based on the binary metal oxide system being investigated. For instance, the $Ir_{(1-x)}Pd_xO_y$ has severe interference between the Pd and O_{1s} spectral lines, the $Ir_{(1-x)}Ru_xO_y$ experiences severe interference due to Ru—C spectral lines, while the $Ir_{(1-x)}Ru_xO_y$ is interfered by the Rh and Ir $4d_{3/2}$ peaks. EDS analysis shows for all single metal and binary metal oxide systems, the coatings are measured to be non-stoichiometric. Specific to the binary metal oxides, the metallic concentration of each constituent metal is observed to strongly influence the amount of oxygen present. As one metal in the binary metal oxide system dominates, the oxygen content is shown to tend towards the oxygen content of that dominant single metal oxide endmember.

The amount of oxygen detected in the IrO_x endmember is considerably greater when compared to that of all $Ir_{(1-x)}Pd_xO_y$ films. The disparity is likely due to the transition from nanoflake and nanoflake-like microstructure to nanospherical microstructure as well as changes in oxidation state of the binary metal oxides. These observations also suggest that the substitution of Pd into metal Ir-lattice sites (and *vice-versa*) strongly influences the chemical bonding occurring in the films and are reflected in the oxygen content.

The oxygen content in the $Ir_{(1-x)}Ru_xO_y$ is notably higher when compared to that of the RuO_x endmember but lower when compared to the IrO_x endmember. The difference in oxygen content in the endmembers could be due to the presence of nanoflake-like microstructure for the IrO_x films and the lack thereof in the RuO_x films. Interestingly, the $Ir_{(1-x)}Ru_xO_y$ films possess oxygen content ≈ 70% regardless of metallic composition which may reflect the oxidation state of the materials.

The oxygen content of $Ir_{(1-x)}Rh_xO_y$ is greater than that of the RhO_x endmember regardless of composition and is generally less than that of the IrO_x endmember. The changes in microstructure and thereby the changes in chemical bonding are likely to strongly influence these variations in oxygen composition. Generally, the oxygen content is lowered with the incorporation of Rh and tends more strongly towards the RhO_x endmember oxygen content values.

3.2.2. XPS

Multiple chemical states are detected in the $Ir_{(1-x)}Pd_xO_y$ system as shown in Table 2. The BE peaks for the endmember PdO_x synthesized under nominally identical conditions are detected at approximately 335.7 and 337.3 eV for the $3d_{5/2}$ spectral line as shown in Fig. 8a. The 335.7 eV BE peak is shifted 0.7 eV higher from the metallic BE peak as shown in Fig. 8a and suggests the presence of an oxide. Indexing of this BE suggests a metallic (Pd^o) or Pd^{2+} oxidation state (PdO) [27] and is

Table 2
$Ir_{(1-x)}Pd_xO_y$ EDS composition and XPS binding energy.[a]

Composition (at.%)			Ir:Pd ratio		$4f_{7/2}$ Position (eV)		$3d_{5/2}$ Position (eV)	
Ir	Pd	O	Ir	Pd	$Ir_{(1-x)}Pd_x^{4+}$	$Ir_{(1-x)}Pd_x^{5+}$	$Ir_{(1-x)}Pd_x^{2+}$	$Ir_{(1-x)}Pd_x^{4+}$
26.66	0	73.34	100%	0%	61.2	61.9	0	0
32.07	5.01	62.93	86%	14%	61.9	63	336.7	338.4
15.44	28.83	55.73	35%	65%	62	62.9	336.8	338.3
4.56	43.41	52.04	10%	90%	62.2	63	337	338.5
3.01	46.52	50.47	6%	94%	61	61.9	337.3	338.8
0	52.58	47.42	0%	100%	0	0	335.7	337.3

[a] Films synthesized at 20% OPP and 30 mTorr WP.

Table 3
$Ir_{(1-x)}Ru_xO_y$ EDS composition and XPS binding energy.[a]

Composition (at.%)			Ir:Ru ratio		$4f_{7/2}$ Position (eV)		$3d_{5/2}$ Position (eV)	
Ir	Ru	O	Ir	Ru	$Ir_{(1-x)}Ru_x^{4+}$	$Ir_{(1-x)}Ru_x^{5+}$	$Ir_{(1-x)}Ru_x^{3/4+}$	$Ir_{(1-x)}Ru_x^{4+}$
26.66	0	73.34	100%	0%	61.2	61.9	0	0
23.95	7.14	68.91	77%	23%	61.9	63	281.3	282.4
20.54	9.46	70.00	68%	32%	61.9	63.1	281.2	282.3
13.44	15.17	71.40	47%	53%	61.9	63.2	281.2	282.3
6.21	22.60	71.19	22%	78%	61.9	63.4	281	282.8
0.00	34.69	65.31	0%	100%	0	0	280.2	282.2

[a] Films synthesized at 20% OPP and 30 mTorr WP.

Table 4
$Ir_{(1-x)}Rh_xO_y$ EDS composition and XPS binding energy.[a]

Composition (at.%)			Ir:Rh ratio		$4f_{7/2}$ Position (eV)		$3d_{5/2}$ Position (eV)	
Ir	Rh	O	Ir	Rh	$Ir_{(1-x)}Rh_x^{4+}$	$Ir_{(1-x)}Rh_x^{5+}$	Rh^o	$Ir_{(1-x)}Rh_x^{3+}$
26.66	0	73.34	100%	0%	61.2	61.9	0	0
22.43	1.83	75.74	92%	8%	61.7	62.6	0	308.5
25.84	9.32	64.84	73%	27%	61.9	62.8	0	308.7
20.55	11.82	67.63	63%	37%	61.9	62.8	0	308.7
4.37	28.94	66.69	13%	87%	62	62.9	0	308.6
0	35.68	64.32	0%	100%	0	0	307.6	308.6

[a] Films synthesized at 20% OPP and 30 mTorr WP.

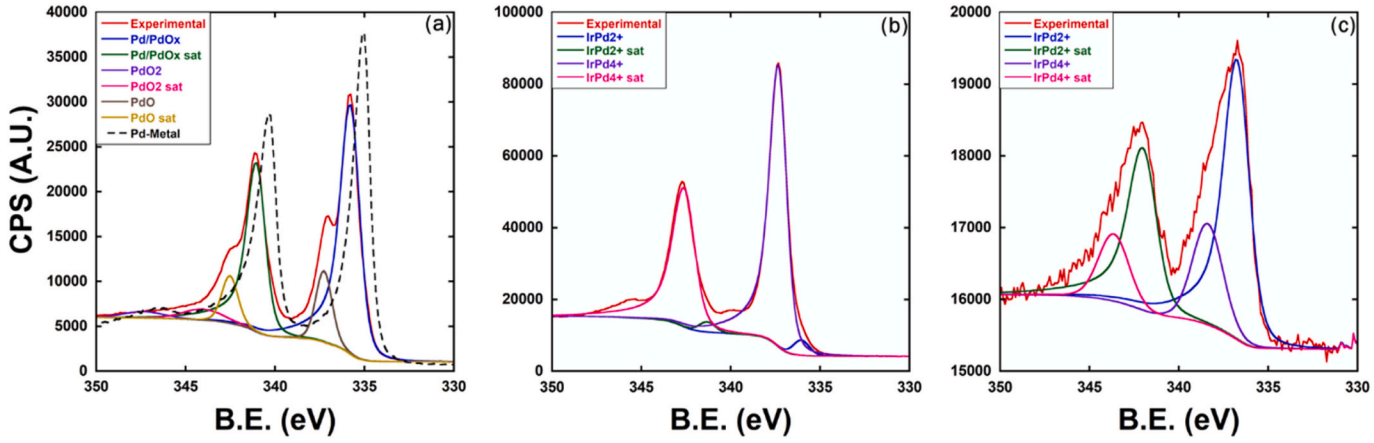

Fig. 8. High resolution XPS spectra and deconvolution analysis of the Pd $3d_{5/2}$ spectral line for (a) PdO_x (b) $Ir_{(0.06)}Pd_{(0.94)}O_y$ (c) $Ir_{(0.86)}Pd_{(0.14)}O_y$ synthesized at 30 mTorr WP and 20% OPP.

assigned Pd/PdO_x. The higher BE peak at 337.3 eV suggests multiple oxidation states primarily Pd^{2+} and Pd^{4+} (PdO_x with $x \leq 2$) and is assigned as PdO_x. Previous XRD analysis on these films indicates the Pd^{2+} oxidation state is dominant in these films [25,26]. The IrO_x end-member BE peaks are detected at 61.2 and 61.9 eV for the $4f_{7/2}$ spectral line as shown in Fig. 9a and provided in Table 2. The lower BE peak can be associated with both Ir-metal (Ir^o) and/or IrO_2 thus it is assigned Ir/IrO_x, while the higher BE peak is less ambiguous and associated closely with the Ir^{4+} (IrO_2) oxidation state of IrO_x and is assigned IrO_x (where $x \leq 2$). Previous XRD analysis suggested that the Ir^{4+} oxidation state is dominant in these coatings [26].

Assuming substitutional replacement of Ir into PdO, dissolving 6% Ir (at.%) in PdO results in notable chemical shifts of the Pd/PdO_x and PdO_x $3d_{5/2}$ BE peaks as shown in Fig. 8b. The Pd/PdO_x experiences a 1.6 eV

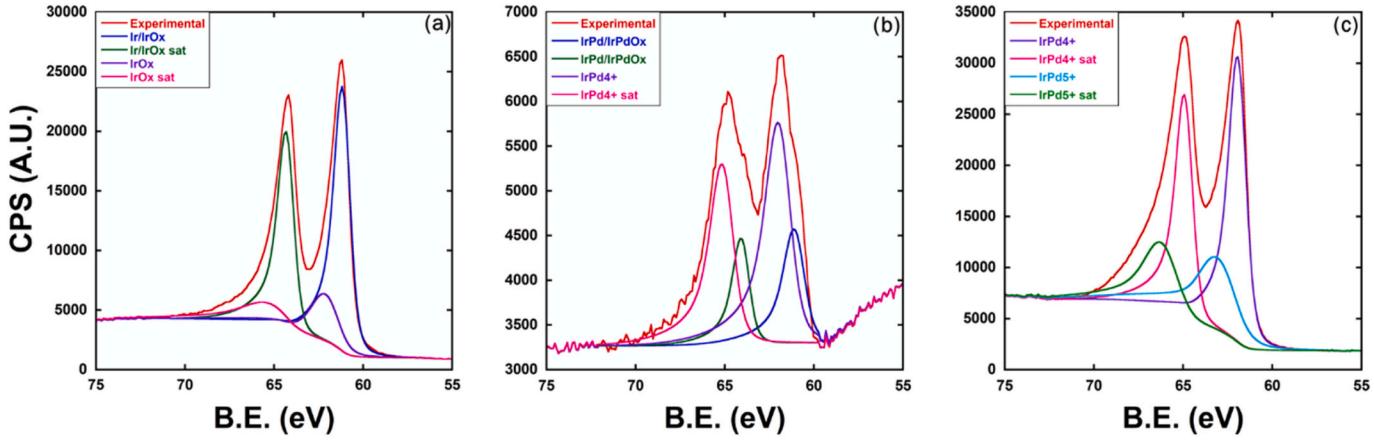

Fig. 9. High resolution XPS spectra and deconvolution analysis of the Ir $4f_{7/2}$ spectral line for (a) IrO_x (b) $Ir_{(0.06)}Pd_{(0.94)}O_y$ (c) $Ir_{(0.86)}Pd_{(0.14)}O_y$ synthesized at 30 mTorr WP and 20% OPP.

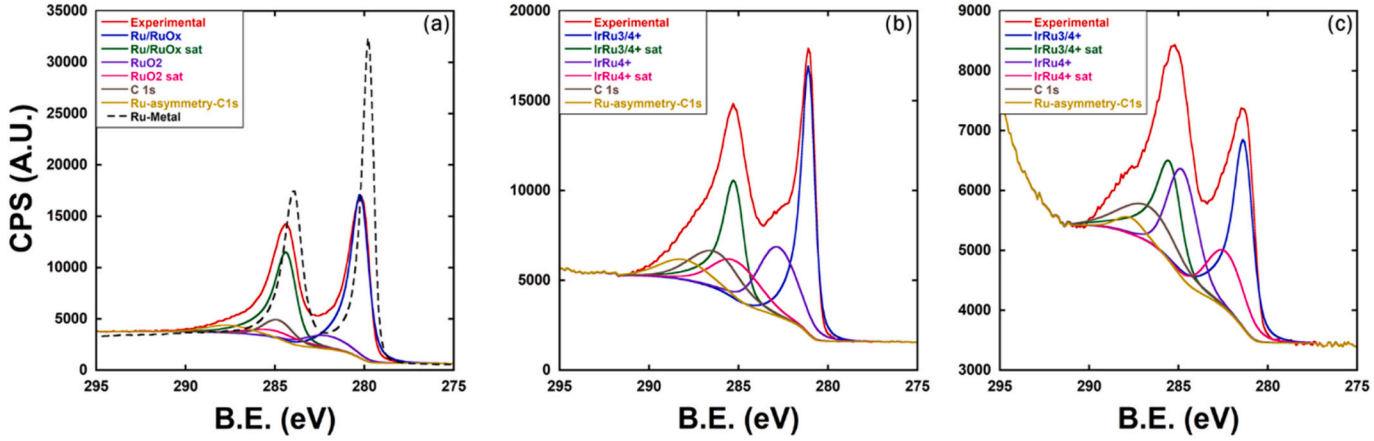

Fig. 10. High resolution XPS spectra and deconvolution analysis of the Ru $3d_{5/2}$ spectral line for (a) RuO_x (b) $Ir_{(0.22)}Ru_{(0.78)}O_y$ (c) $Ir_{(0.77)}Ru_{(0.23)}O_y$ synthesized at 30 mTorr WP and 20% OPP.

positive shift from 335.7 and 337.3 eV, while the PdO_x peak positively shifts by 1.5 eV from 337.3 and 338.8 eV. The Pd/PdO_x is reassigned to $Ir_{(1-x)}Pd_xO_y$ where $y \leq 1$, the shifted BE suggests the presence of a + 2 oxidation state for the binary metal oxide films. Additionally, this $Ir_{(1-x)}Pd_x^{2+}$ BE peak is shown to negatively shift with increasing Ir-metal concentration somewhat systemically and thereby acts as an indicator to the changing chemical bonding characteristics of the binary metal oxide solid solutions. This systematic shift is suspected to be related to the chemical bonding and oxidation state changes that are a result of the difference in the native oxidation states of the endmember single metal oxides *i.e.*, Pd^{2+} and Ir^{4+}. The previously assigned PdO_x BE peak is reassigned to $Ir_{(1-x)}Pd_x^{4+}$ as shown in Fig. 8c and is believed to be related to the +4 oxidation state of the $Ir_{(1-x)}Pd_xO_y$ films, thus in this case $y \leq 2$ for this solid solution. Notably, the BEs of the $Ir_{(1-x)}Pd_x^{4+}$ are distinctly greater than the BEs measured for the endmember Pd^{4+} oxidation state [27] which may suggest that higher oxidation states are present. Similar to the $Ir_{(1-x)}Pd_x^{2+}$ BE peaks, $Ir_{(1-x)}Pd_x^{4+}$ peaks undergo negative chemical shifts with increasing Ir-metallic content; however, the +4 peaks shifts are not systematic. This may indicate a stable chemical state is present. On the opposite end, the Ir-related $4f_{7/2}$ BE peaks experience a positive chemical shift with increasing Pd-content (so long as $0 < x < 0.94$) when compared to that the of the IrO_x endmember as shown in Fig. 9b and c and provided in Table 2. The lower energy peak previously assigned to Ir/IrO_x experiences a ≈0.7 eV positive chemical shift, while the IrO_x peak undergoes a 1.1 eV positive shift. The lower energy peak is assigned to $Ir_{(1-x)}Pd_x^{4+}$ as it matches closely with the Ir^{4+} oxidation state BE peak. The notably higher BE of the IrO_x peak previously associated primarily with Ir^{4+} may suggest a +5 oxidation state of $Ir_{(1-x)}Pd_xO_y$ (for $0 < x < 0.94$) and is assigned as $Ir_{(1-x)}Pd_x^{5+}$.

The XPS results for the $Ir_{(1-x)}Ru_xO_y$ system are presented in Table 3. Unlike the single metal oxide endmembers for the $Ir_{(1-x)}Pd_xO_y$ system which had differing native oxidations states, the native oxidation state of both endmembers oxides is +4. The $3d_{5/2}$ spectral line relating to the RuO_x endmember is indexed and the spectra are presented in Fig. 10a. The lower BE (280.1 eV) is assigned to the non-stoichiometric oxide Ru/RuO_x, while the higher BE peak located at 282.2 eV indicates the presence of Ru^{4+} species (RuO_2) [27]. The Ru/RuO_x BE peak undergoes a positive chemical shift from 280.1 to approximately 281.2 eV ± 0.1 when at least 22% Ir (at.%) is substituted in the RuO_x Ru metal lattice sites as shown in Fig. 10b. The greater BE of the $Ir_{(1-x)}Ru_xO_y$ when compared to that of the single metal oxide endmember suggests a combination of +3 and +4 oxidation state are likely present, therefore the Ru/RuO_x peak is reassigned to $Ir_{(1-x)}Ru_x^{3/4+}$. Interestingly, a small but incremental positive chemical shift is identified in the $3d_{5/2}$ $Ir_{(1-x)}Ru_x^{4+}$ spectral line with increasing Ir-content, this may indicate a change in the chemical bonding of the binary metal oxide as one endmember metal becomes dominant. Initially, a 0.6 eV positive shift is observed in the higher energy $3d_{5/2}$ spectral line previously assigned to the Ru^{4+} oxidation state occurs when $x = 0.78$ (22 at.%. Ir) the spectral line shifts back towards the Ru^{4+} endmember value with increased Ir-content ($x < 0.78$). This transition is believed to be related to the change in chemical bonding from a primary solid solution where RuO_x is

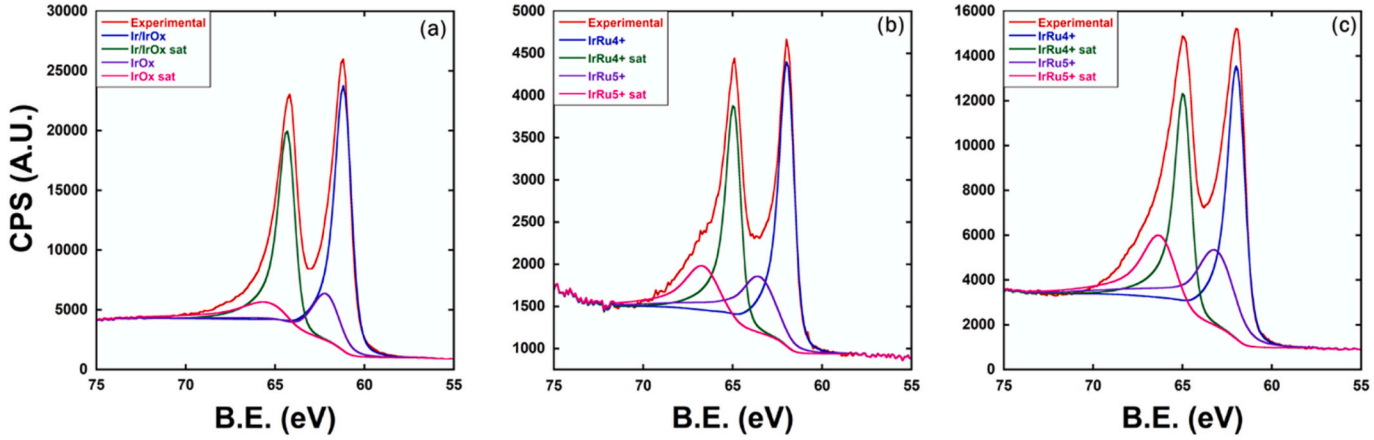

Fig. 11. High resolution XPS spectra and deconvolution analysis of the Ir $4f_{7/2}$ spectral line for (a) IrO_x (b) $Ir_{(0.22)}Ru_{(0.78)}O_y$ (c) $Ir_{(0.77)}Ru_{(0.23)}O_y$ synthesized at 30 mTorr WP and 20% OPP.

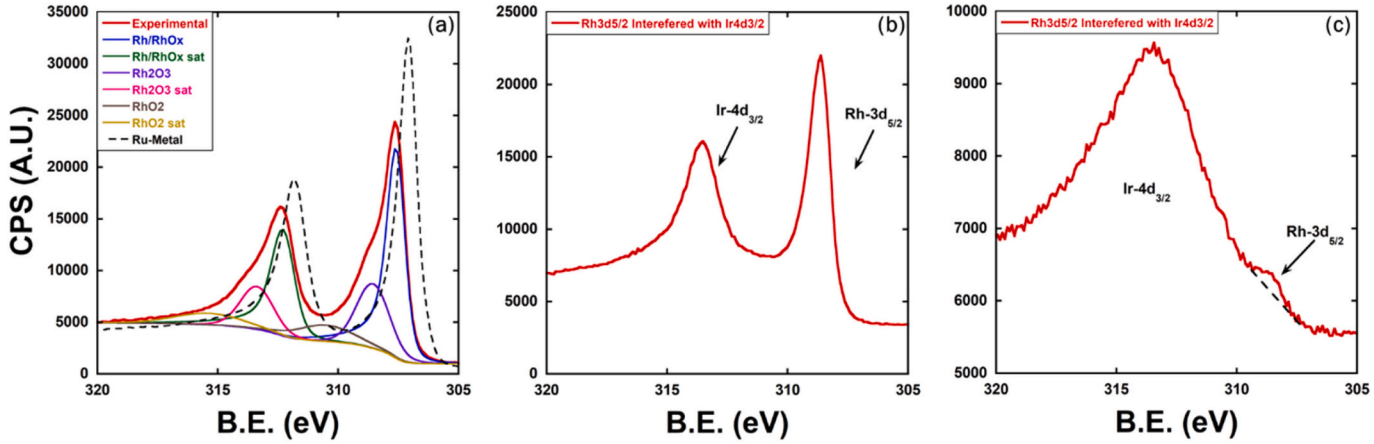

Fig. 12. High resolution XPS spectra and deconvolution analysis of the Rh $3d_{5/2}$ spectral line for (a) RhO_x (b) $Ir_{(0.13)}Rh_{(0.87)}O_y$ (c) $Ir_{(0.92)}Rh_{(0.08)}O_y$ synthesized at 30 mTorr WP and 20% OPP.

dominant to a less structured intermediate solid solution. Nonetheless, because this spectral line remains close to that of the Ru^{4+} BE peak it is appropriate to reassign it to $Ir_{(1-x)}Ru_x^{4+}$ for the binary metal solid solution. A positive chemical shift of approximately 0.7 eV (61.9 eV) is observed in the $4f_{7/2}$ spectral line previously assigned to Ir/IrO_x. Interestingly, this BE peak does not fluctuate in value with changing composition for the $Ir_{(1-x)}Ru_xO_y$ system suggesting a stable bonding characteristic for this chemical state. This shifted BE is associated with the Ir^{4+} oxidation, and thus is assigned as $Ir_{(1-x)}Ru_x^{4+}$ for the $Ir_{(1-x)}Ru_xO_y$ system. These BEs are shown to be invariant with composition. The higher BE (61.9 eV) $4f_{7/2}$ previously assigned to IrO_x ($x \leq 2$) is positively chemically shifted to higher BEs for the $Ir_{(1-x)}Ru_xO_y$ system. This shift is

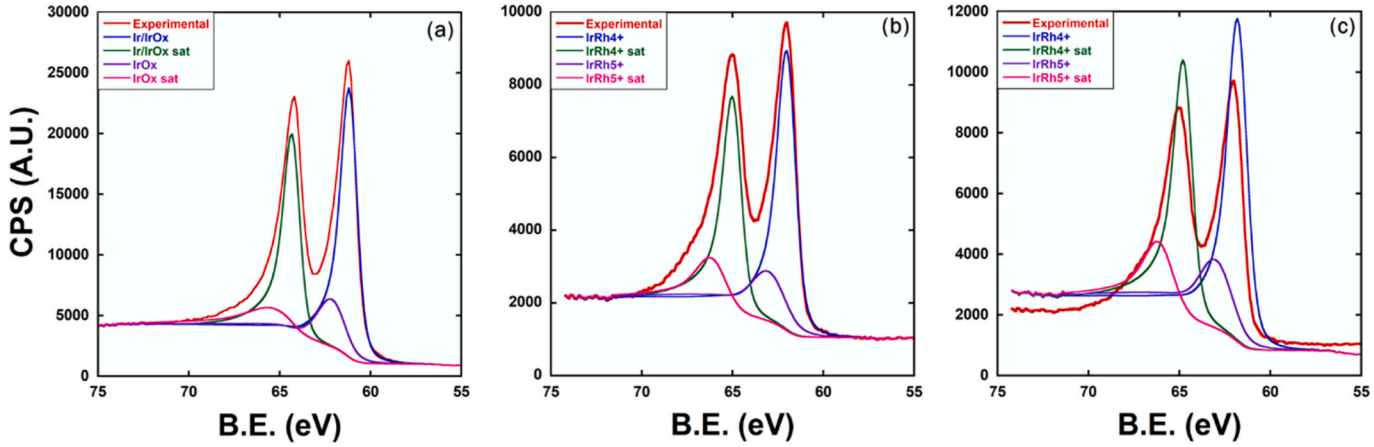

Fig. 13. High resolution XPS spectra and deconvolution analysis of the Ir $4f_{7/2}$ spectral line for (a) RhO_x (b) $Ir_{(0.13)}Rh_{(0.87)}O_y$ (c) $Ir_{(0.92)}Rh_{(0.08)}O_y$ synthesized at 30 mTorr WP and 20% OPP.

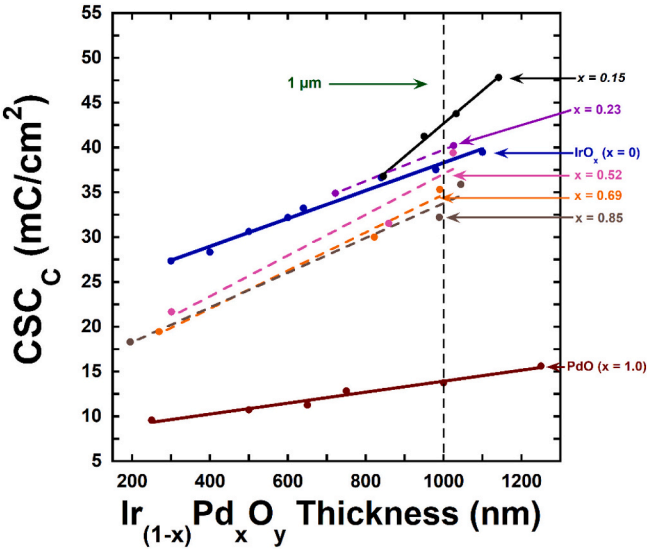

Fig. 14. CSC_C as a function of film thickness of $Ir_{(1-x)}Pd_xO_y$ using the natural thickness gradient from the combinatorial approach selected. (ν = 0.1Vs 1, 0.1 M PBS solution, GSA ≈ 0.46 cm^2, reference Ag|AgCl).

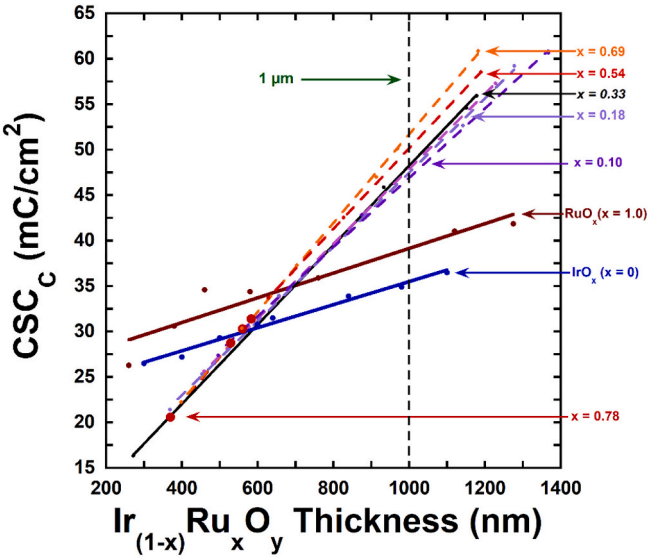

Fig. 16. CSC_C as a function of thickness in $Ir_{(1-x)}Ru_xO_y$ films exhibiting a thickness dependent gradient. (ν = 0.1Vs 1, 0.1 M PBS solution, GSA ≈ 0.46 cm^2, reference Ag|AgCl).

incremental, when x = 0.23 the chemical shift is 1.1 eV as shown in Fig. 11c (when compared to that of the IrO_x endmember) and further increases with increasing Ru-content (Fig. 11b). While previously associated with the Ir^{4+} oxidation state, this positive chemical shift suggests that higher oxidation states are likely present in the $Ir_{(1-x)}Ru_xO_y$ system and thus this spectral line is assigned as $Ir_{(1-x)}Ru_x^{5+}$. Based on stoichiometry, the oxygen content as measured by EDS for these films is in general agreement with the presence of a +5 oxidation state.

The BEs for the $Ir_{(1-x)}Rh_xO_y$ system are provided in Table 4. Similar to the other binary metal oxides in this study, multiple chemical states are present. The $3d_{5/2}$ RhO_x endmember spectral lines indicate that both metallic and oxide are present as shown in Fig. 12a. Two Rh-related peaks are present, a metallic Rh peak (Rh^o) at a BE of 307.6 eV, and a RhO_x at a BE of 308.6 eV. The oxide peak matches with +3 oxidation state and is therefore assigned as Rh^{3+}. Due to the previously mentioned severe interference shown in Fig. 12b and c, the speciation of the $Ir_{(1-x)}Rh_xO_y$ films using the Rh spectral lines is difficult. Nonetheless, for the BE peaks which are discernable in the $Ir_{(1-x)}Rh_xO_y$, the previously assigned Rh^{3+} endmember BE peak is present and is therefore assigned as $Ir_{(1-x)}Rh_x^{3+}$ for the $Ir_{(1-x)}Rh_xO_y$ system. The Ir-related $4f_{7/2}$ BE peaks are much more manageable and are shown to undergo positive chemical shifts with increasing Rh-content as shown in Fig. 13b and c and presented in Table 4. The Ir/IrO_x assigned peak shifts towards the Ir^{4+} value and is therefore assigned as $Ir_{(1-x)}Rh_x^{4+}$ for the $Ir_{(1-x)}Rh_xO_y$ system. The IrO_x BE peak primarily associated with the Ir^{4+} oxidation state similarly shifts to what is likely a higher oxidation state and is therefore assigned as $Ir_{(1-x)}Rh_x^{5+}$. Similar to the other two binary metal oxide systems, these BE peaks that shift with metallic concentration are likely related to the changing chemical bonding characteristics based on the solubility of each metal into the other metals lattice sites.

3.3. Cyclic voltammetry

The CSC_C of $Ir_{(1-x)}Pd_xO_y$ films as a function of composition and thickness are presented in Fig. 14. Generally, the CSC_C trends upward with decreasing Pd-concentrations with all compositions possessing superior electrochemical performance when compared to that of the pure PdO. On the other hand, only compositions where x ≥ 0.23 possess

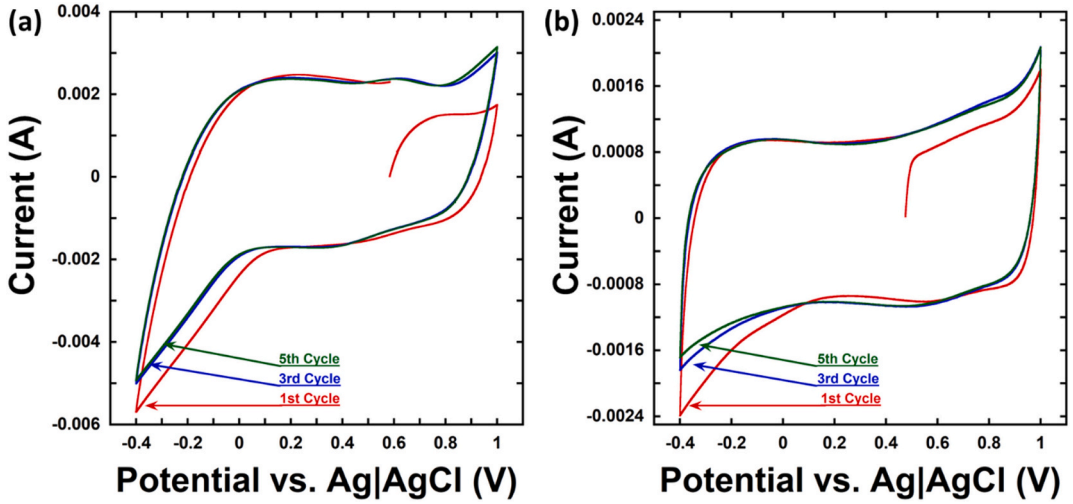

Fig. 15. Typical cyclic voltammograms (1st, 3rd, and 5th cycle) of (a) $Ir_{(0.84)}Pd_{(0.16)}O_y$, (b) $Ir_{(0.06)}Pd_{(0.94)}O_y$, deposited on 316 SS substrates and synthesized at 20% OPP and 30 mTorr WPs. (ν = 0.1Vs 1, 0.1 M PBS solution, GSA ≈ 0.46 cm^2, reference Ag|AgCl).

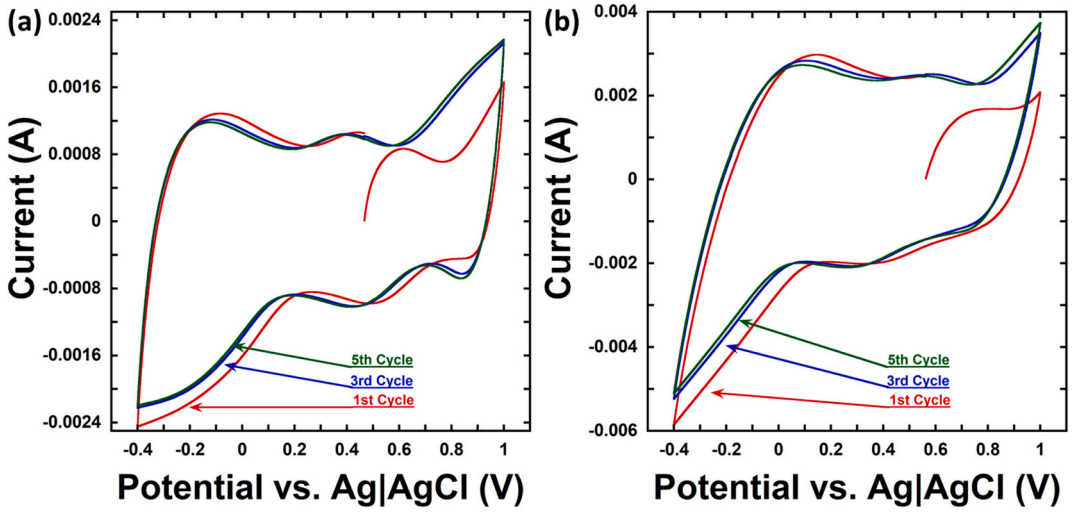

Fig. 17. Typical cyclic voltammograms (1st, 3rd, and 5th cycle) of (a) $Ir_{(0.77)}Ru_{(0.23)}O_y$, (b) $Ir_{(0.22)}Ru_{(0.78)}O_y$, deposited on 316 SS substrates and synthesized at 20% OPP and 30 mTorr WPs. (ν = 0.1Vs 1, 0.1 M PBS solution, GSA ≈ 0.46 cm^2, reference Ag|AgCl).

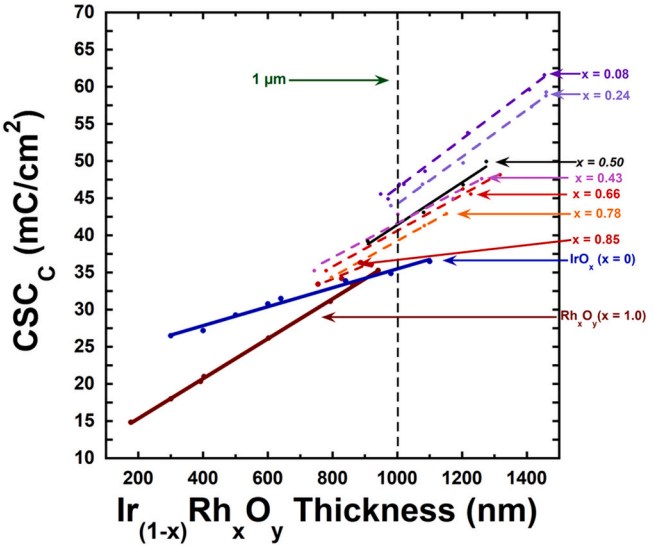

Fig. 18. CSC_C as a function of thickness in $Ir_{(1-x)}Rh_xO_y$ films exhibiting a thickness dependent gradient. (ν = 0.1Vs 1, 0.1 M PBS solution, GSA ≈ 0.46 cm^2, reference Ag|AgCl).

superior electrochemical performance over pure IrO_x. The CSC_C data also suggests that at compositions where Pd is assumed to be close to its solubility limit in the IrO_x metal lattice sites *i.e.*, x ≈ 0.15, the CSC_C exceeds all other compositions for thicknesses greater than or equal to 800 nm. The difference in the slope of the CSC_C observed at x ≈ 0.15 may be related to changes in film morphology and microstructure that occur at this threshold. Representative cyclic voltammograms for the $Ir_{(1-x)}Pd_xO_y$ system are shown in Fig. 15a and b for high Ir and high Pd-content films, respectively. In both cases the cyclic voltammograms are shown to stabilize following the initial scan. The relative difference of the initial scan is likely related to the oxygen trapped in the solution (the PBS solution was not explicitly deaerated) and in the film. Additionally, the presence of small amounts of unreacted metal may also be a contributing factor to the variation in the initial scan, however, the subsequent scans suggest that films are nearly or completely oxidized when grown.

The CSC_C values for the $Ir_{(1-x)}Ru_xO_y$ films as functions of composition and thickness are presented in Fig. 16. The slope of the CSC_C as a function of thickness of each composition of $Ir_{(1-x)}Ru_xO_y$ was greater than that of the single metal oxides. Additionally, the cross-over thicknesses where the binary metal oxide system exceeds the electrochemical performance of the pure oxides were approximately 600 nm, and 600–700 nm, for IrO_x and RuO_x, respectively. At 1 µm the electrochemical performance of the $Ir_{(1-x)}Ru_xO_y$ films was considerably greater than that of either of the single metal oxides. Furthermore, the CSC_C improved as Ru content in the films increased. The representative cyclic voltammograms for the $Ir_{(1-x)}Ru_xO_y$ system are presented in Fig. 17a and b for high Ir and high Ru-content, respectively. Similar to the $Ir_{(1-x)}Pd_xO_y$ oxide system, the initial scan differs somewhat in comparison to that of the 3rd and 5th scans with similar explanation as previously discussed. Upon the third sweep for both compositions the voltammogram is shown to be extremely stable, showing very little fluctuation in the curve shape, peak current height, and peak potential locations. These characteristics strongly suggest that over the potential scan range and number of cycles tested the $Ir_{(1-x)}Ru_xO_y$ are oxidized prior to cyclic voltammetry (*i.e.*, during growth) and are electrochemically stable.

The CSC_C as a function of thickness and composition of the $Ir_{(1-x)}Rh_xO_y$ films is presented in Fig. 18. The $Ir_{(1-x)}Rh_xO_y$ solid solutions exhibited superior electrochemical performance when compared to either of the single metal oxides at thicknesses above 750 nm. Generally, as the Rh content is increased the electrochemical performance is reduced in the $Ir_{(1-x)}Rh_xO_y$. The highest performing films are those that are dominated by nanoflake growth (x = 0.08 and 0.24). Those films dominated by nano-spherical growth while exhibiting nanoflake microstructure (x = 0.43) showed similar electrochemical performance to films that formed large clusters of nanospherical grains (x ≈ 0.50). The slope of the CSC_C as a function of thickness is shown to change at a rate between those of the single oxides. Similar to the other two binary oxide systems, representative CV curves for the $Ir_{(1-x)}Rh_xO_y$ are shown in Fig. 19a and b for high Ir and high Rh-content films, respectively. A comparable response in the CV curves is observed in the $Ir_{(1-x)}Rh_xO_y$ to that of the other two binary metal oxides. The evolution of the curves suggests the films are electrochemically stable, possess insignificant amounts of unreacted metal, and as a result are likely nearly or fully oxidized when synthesized.

4. Discussion

The solubility limit of each metal into the host metal oxide lattice can be inferred from the micrographs, and knowledge of their respective compositions. These solubility limits are consistent with XRD

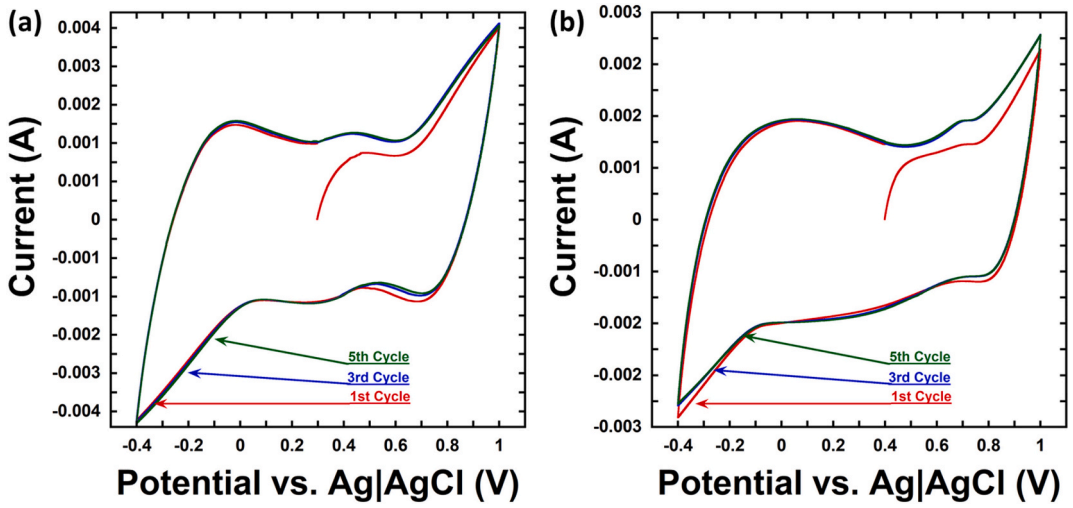

Fig. 19. Typical cyclic voltammograms (1st, 3rd, and 5th cycle) of (a) $Ir_{(0.92)}Rh_{(0.08)}O_y$, (b) $Ir_{(0.13)}Rh_{(0.87)}O_y$, deposited on 316 SS substrates and synthesized at 20% OPP and 30 mTorr WPs. (ν = 0.1Vs 1, 0.1 M PBS solution, GSA ≈ 0.46 cm^2, reference Ag|AgCl).

observations in previous work in the binary metal oxide systems [25,26]. The Hume-Rothery rules, which describe the solubility of an element into a metal to form a solid solution, can be applied to these metal oxide systems with some additional considerations [28–31]. These rules suggest that there will be limited solubility of Pd into IrO_x and *vice-versa*. For instance, Pd^{2+} dissolving into the lattice position of Ir^{4+} will result in a cation vacancy and thereby a non-neutral crystal structure with two uncompensated electrons (*i.e.*, one O^{2-}). As a consequence, adjacent Ir^{4+} could be reduced to Ir^{2+} or Pd could be oxidized further to Pd^{4+} to maintain charge neutrality. In the case of Pd dissolving into IrO_x Ir metal lattice sites, the creation of oxygen vacancies is expected to occur in order to balance uncompensated charge. Additionally, the size factor and valency (considering the ionic radii of the assumed oxidation states) are also likely to play a meaningful role in the solubility of the metals. Regardless of the charge compensation that occurs, these substitutional defects due to differences in native oxidation states, and the criteria expressed in the Hume-Rothery rules strongly influence the resultant microstructure of the binary metal oxide films. While defects are likely and expected in these films, further testing is required to investigate the prevalence and nature of the defects that develop in these binary metal oxides films as a function of metallic composition.

The XPS results were shown to provide key insights into the changing chemical state of the coatings. When compared to the single metal oxide endmembers, the binary metal oxides in general resulted in considerable positive shifts in the comparable spectral line BEs. In many cases the positive shifts exceeded the BE of known oxidations states of the single metal oxide endmember indicating activation of higher oxidation states in the binary metal oxides. The nature of this oxidation could be a result of charge compensation resulting from substitutional defects which depend on the various characteristics of the endmembers previously discussed. Additionally, multiple chemical states were identified to be present in the binary metal oxide films, some spectral lines were shown to shift systemically with increasing/decreasing metallic concentration, some examples of this behavior include the $Ir_{(1-x)}Pd_x^{2+}$ $3d_{5/2}$ spectral line, $Ir_{(1-x)}Ru_x^{5+}$ $4f_{7/2}$ spectral line, and the $Ir_{(1-x)}Rh_x^{5+}$ $4f_{7/2}$ spectral line. This behavior may indicate that some chemical species present in the binary metal oxide films are less chemically stable and will be oxidized and reduced or change chemical bonding more readily based on metallic concentration.

Nanoflake growth has been associated with the (011) surface of rutile IrO_2 (Ir^{4+}) and has been shown to develop under higher surface energy conditions [26]. The minimum compositional ranges required to suppress nanoflake growth while maintaining improved electrochemical performance for each of the binary $Ir_{(1-x)}M_xO_y$ metal oxide systems have been identified. Each binary metal oxide system required different solute concentrations in order to transition from a primary solid solution while exhibiting nanoflake structure to an intermediate solid solution structure with a different crystal structure based on microstructural characteristics. Similar concentration limits have been identified for Ir into the MO_x lattice. The solute concentrations required for the microstructural transitions to occur are broadly described by the Hume-Rothery rules (with additional considerations for ceramic systems) and substitutional defect effects [32–34]. Among the three binary metal oxide systems, the $Ir_{(1-x)}Pd_xO_y$ required the least (x ≈ 0.14), while the $Ir_{(1-x)}Rh_xO_y$ system required the greatest (x ≈ 0.50) amount of M metal for suppression of nanoflakes. In all cases, these values are likely related to the substitutional solubility limits of each element into the host oxide's metal lattice sites.

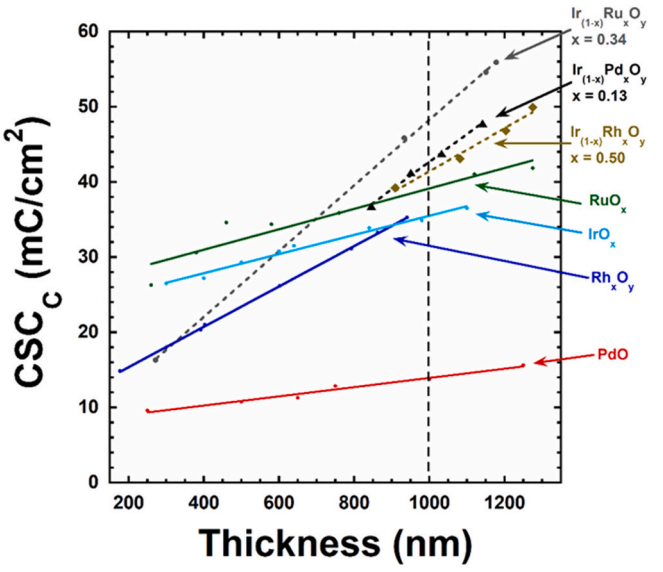

Fig. 20. CSC_C as a function of film thickness for the primary solubility limit compositions of the binary metal oxides; The results from the single metal oxide endmembers are included for comparison. (ν = 0.1Vs 1, 0.1 M PBS solution, GSA ≈ 0.46 cm^2, reference Ag|AgCl).

The electrochemical performance as measured by CV for all binary metal oxides improved with increased film thickness, and each voltammogram suggested the films were electrochemically stable. This

characteristic is attributed to the morphology that results from the sputtering pressure conditions [35–39]. Generally, the slopes of the CSC_C as a function of thickness for each binary metal oxide system were greater than that of their single metal oxide endmember. As a consequence, film thickness had a greater contribution to electrochemical performance such that the binary metal oxides were only able to outperform their single metal oxide endmembers if grown above specific thicknesses. For the $Ir_{(1-x)}Rh_xO_y$ and $Ir_{(1-x)}Ru_xO_y$ systems, all compositions outperformed their single metal oxide endmembers if grown to thicknesses $\geq$ 750 nm. However, only two compositions (x = 0.15 and 0.23) for the $Ir_{(1-x)}Pd_xO_y$ system were able to electrochemically outperform both endmembers and only if grown at thicknesses $\geq$ 800 nm. Direct comparison of the electrochemical performance of the binary metal oxides at 1 μm thicknesses and which possess chemical composition near or at the assumed primary solubility limits of the M metal (Fig. 20) indicate that, the systems with the strongest to weakest performance are $Ir_{(1-x)}Ru_xO_y$, $Ir_{(1-x)}Pd_xO_y$, and $Ir_{(1-x)}Rh_xO_y$, respectively. In addition to the thickness dependence, high resolution XPS revealed that the binary metal oxides were seemingly have higher activated oxidation states when compared to that of their single metal oxide endmembers. It is suspected that the activation of these higher oxidation states are strong contributors to the improved performance of the binary metal oxide films, with the most obvious case being the $Ir_{(1-x)}Pd_xO_y$ system. Therefore, somewhat unsurprisingly, films which possess a greater abundance of higher activated oxidation states will have better charge exchange. Microstructure and chemical state are deemed to be determining characteristics that contribute to the electrochemical performance of the single and binary metal oxide films. However, it is likely that the defects in the crystal structure of the films also have a contributing role in electrochemical performance, thus more work is required to better deconvolute these factors.

5. Conclusions

The microstructural and electrochemical characteristics of the binary metal oxides were demonstrated to be generally more desirable than those of their single metal oxide endmembers. This is particularly important with respect to suppression of nanoflake growth in the IrO_x primary solid solution regions of the binary metal oxides. Importantly, the solute concentration for each binary metal oxide which suppressed nanoflake growth were identified and found to be approximately $x \geq 0.13$, $x \geq 0.34$, and $x \geq 0.50$, for $Ir_{(1-x)}Pd_xO_y$, $Ir_{(1-x)}Ru_xO_y$, and $Ir_{(1-x)}Rh_xO_y$, respectively. In addition, the activation of higher oxidation states including a +5 oxidation state in the binary metal oxide systems are believed to be key characteristic contributing to the enhanced performance of these films over the single metal oxide endmembers. The desirable microstructures and favorable electrochemical characteristics observed in these binary metal oxide systems demonstrate that these materials are strong candidates for further testing for use in implantable neural interfacing applications.

CRediT authorship contribution statement

Gregory Taylor: Conceptualization, Methodology, Software, Validation, Formal analysis, Investigation, Writing – original draft, Writing – review & editing, Visualization, Supervision. **Jeffrey Shallenberger:** Investigation, Formal analysis, Writing – review & editing. **Saxon Tint:** Resources, Supervision. **Andrew Fones:** Writing – review & editing, Validation. **Hugh Hamilton:** Writing – review & editing. **Lei Yu:** Conceptualization, Methodology, Writing – review & editing. **Shahram Amini:** Conceptualization, Writing – review & editing, Resources. **Jeffrey Hettinger:** Conceptualization, Methodology, Writing – review & editing, Resources.

Declaration of competing interest

The authors declare that they have no known competing financial interests or personal relationships that could have appeared to influence the work reported in this paper.

Acknowledgements

The authors acknowledge a National Science Foundation instrumentation grant (CBET-MRI-1625816). This work was partially supported by National Science Foundation through the Penn State University MRSEC DMR 1420620 & MRSEC DMR 2011839. All XPS analyses were performed at the Penn State Materials Characterization Laboratory as part of the MRFN program. We thank Theodore Scabarozi and Carl Lunk and for their assistance with instrumentation.

Appendix A. Supplementary data

Supplementary data to this article can be found online at https://doi.org/10.1016/j.surfcoat.2021.127803.

References

[1] J.M. Ferguson, SSRI antidepressant medications: adverse effects and tolerability, Prim. Care Companion J. Clin. Psychiatry 3 (2001) 22–27.
[2] L.F. Chu, D.J. Clark, M.S. Angst, Opioid tolerance and hyperalgesia in chronic pain patients after one month of oral morphine therapy: a preliminary prospective study, J. Pain 7 (2006) 43–48, https://doi.org/10.1016/j.jpain.2005.08.001.
[3] M.M. Morgan, M.J. Christie, Analysis of opioid efficacy, tolerance, addiction and dependence from cell culture to human, Br. J. Pharmacol. 164 (2011) 1322–1334, https://doi.org/10.1111/j.1476-5381.2011.01335.x.
[4] A. Alkaaki, O.O. Al-Radi, A. Khoja, A. Alnawawi, A. Alnawawi, A. Maghrabi, A. Altaf, M. Aljiffry, Surgical site infection following abdominal surgery: a prospective cohort study, Can. J. Surg. 62 (2019) 111–117, https://doi.org/10.1503/cjs.004818.
[5] F. Sattar, Z. Sattar, M. Zaman, S. Akbar, Frequency of post-operative surgical site infections in a tertiary care hospital in Abbottabad, Pakistan, Cureus. 11 (n.d.) e4243. doi:https://doi.org/10.7759/cureus.4243.
[6] D.E. Reichman, J.A. Greenberg, Reducing surgical site infections: a review, Rev. Obstet. Gynecol. 2 (2009) 212–221.
[7] Y. Wang, S. Vaddiraju, B. Gu, F. Papadimitrakopoulos, D.J. Burgess, Foreign body reaction to implantable biosensors: effects of tissue trauma and implant size, J. Diabetes Sci. Technol. 9 (2015) 966–977, https://doi.org/10.1177/1932296815601869.
[8] H. Akhtar, F. Bukhari, M. Nazir, M.N. Anwar, A. Shahzad, Therapeutic efficacy of neurostimulation for depression: techniques, current modalities, and future challenges, Neurosci. Bull. 32 (2016) 115–126, https://doi.org/10.1007/s12264-015-0009-2.
[9] A.L. Benabid, Deep brain stimulation for Parkinson's disease, Curr. Opin. Neurobiol. 13 (2003) 696–706, https://doi.org/10.1016/j.conb.2003.11.001.
[10] P. Davis, J. Gaitanis, Neuromodulation for the treatment of epilepsy: a review of current approaches and future directions, Clin. Ther. 42 (2020) 1140–1154, https://doi.org/10.1016/j.clinthera.2020.05.017.
[11] B.C. Albensi, treatments (non-antiepileptic drugs)|electrical stimulation, in: P. A. Schwartzkroin (Ed.), Encyclopedia of Basic Epilepsy Research, Academic Press, Oxford, 2009, pp. 1426–1430, https://doi.org/10.1016/B978-012373961-2.00002-3.
[12] A. Baldini, M. Von Korff, E.H.B. Lin, A review of potential adverse effects of long-term opioid therapy: a practitioner's guide, Prim. Care Companion CNS Disord. 14 (2012), https://doi.org/10.4088/PCC.11m01326.
[13] A. Bourrier, Graphene Bioelectronics for Long Term Neuronal Interfacing In-Vivo, (n.d.) 199.
[14] G. Guitchounts, J.E. Markowitz, W.A. Liberti, T.J. Gardner, A carbon-fiber electrode array for long-term neural recording, J. Neural Eng. 10 (2013), 046016, https://doi.org/10.1088/1741-2560/10/4/046016.
[15] K.A. Sillay, S. Ondoma, B. Wingeier, D. Schomberg, P. Sharma, R. Kumar, G. S. Miranpuri, J. Williams, Long-term surface electrode impedance recordings associated with gliosis for a closed-loop neurostimulation device, Ann. Neurosci. 25 (2018) 289–298, https://doi.org/10.1159/000481805.
[16] M. Leber, R. Bhandari, J. Mize, D.J. Warren, M.M.H. Shandhi, F. Solzbacher, S. Negi, Long term performance of porous platinum coated neural electrodes, Biomed. Microdevices 19 (2017) 62, https://doi.org/10.1007/s10544-017-0201-4.
[17] R. Atmaramani, B. Chakraborty, R.T. Rihani, J. Usoro, A. Hammack, J. Abbott, P. Nnoromele, B.J. Black, J.J. Pancrazio, S.F. Cogan, Ruthenium oxide based microelectrode arrays for in vitro and in vivo neural recording and stimulation, Acta Biomater. 101 (2020) 565–574, https://doi.org/10.1016/j.actbio.2019.10.040.
[18] M. Gulino, D. Kim, S. Pané, S.D. Santos, A.P. Pêgo, Tissue response to neural implants: the use of model systems toward new design solutions of implantable

microelectrodes, Front. Neurosci. 13 (2019), https://doi.org/10.3389/fnins.2019.00689.
[19] J. Ordonez, M. Schuettler, C. Boehler, T. Boretius, T. Stieglitz, Thin films and microelectrode arrays for neuroprosthetics, MRS Bull. 37 (2012) 590–598, https://doi.org/10.1557/mrs.2012.117.
[20] S.M. Wellman, J.R. Eles, K.A. Ludwig, J.P. Seymour, N.J. Michelson, W. E. McFadden, A.L. Vazquez, T.D.Y. Kozai, A materials roadmap to functional neural interface design, Adv. Funct. Mater. 28 (2018), https://doi.org/10.1002/adfm.201701269.
[21] C. Boehler, S. Carli, L. Fadiga, T. Stieglitz, M. Asplund, Tutorial: guidelines for standardized performance tests for electrodes intended for neural interfaces and bioelectronics, Nat. Protoc. 15 (2020) 3557–3578, https://doi.org/10.1038/s41596-020-0389-2.
[22] K. Göbbels, T. Kuenzel, A. van Ooyen, W. Baumgartner, U. Schnakenberg, P. Bräunig, Neuronal cell growth on iridium oxide, Biomaterials. 31 (2010) 1055–1067, https://doi.org/10.1016/j.biomaterials.2009.10.029.
[23] B. Wessling, Sputter deposition of iridium and iridium oxide for stimulation electrode coatings. https://core.ac.uk/display/36429124, 2007. (Accessed 10 June 2020).
[24] S.-A. Park, K.-S. Kim, Y.-T. Kim, Electrochemically activated iridium oxide black as promising electrocatalyst having high activity and stability for oxygen evolution reaction, ACS Energy Lett. 3 (2018) 1110–1115, https://doi.org/10.1021/acsenergylett.8b00368.
[25] S. Amini, J.D. Hettinger, G. Taylor, Thin film coating. https://patentscope.wipo.int/search/en/detail.jsf?docId=WO2020240193&tab=PCTBIBLIO&_cid=P22-KI9023-43389-1, 2020. (Accessed 19 December 2020).
[26] G. Taylor, Investigation of Single, Binary, and Ternary Metal Oxides of Iridium, Rhodium, and Palladium for Neural Interfacing Applications, Theses and Dissertations, https://rdw.rowan.edu/etd/2918, 2021.
[27] A. Naumkin, A. Vass-Kraut, S. Gaarenstroom, C. Powell, X-ray Photoelectron Spectroscopy Database XPS,Version 4.1, NIST Standard Reference Database 20, 2012, https://doi.org/10.18434/T4T88K.
[28] M. Ahlers, The Hume-Rothery rules and phase stabilities in noble metal alloys, Z. Phys. B Condens. Matter 99 (1995) 491–499, https://doi.org/10.1007/BF02769972.
[29] L. Battezzati, Solid Solutions in Metals: From Hume-Rothery's Rules to High Entropy Alloys, (n.d.) 16.
[30] S.C. Bayne, J.Y. Thompson, CERAMICS: Properties 1 (Physical, Chemical, Mechanical), (n.d.) 10.
[31] C.B. Carter, M.G. Norton, Ceramic Materials: Science and Engineering, Springer Science & Business Media, 2007.
[32] J.J. Quinn, K.-S. Yi, Solid State Physics, Springer International Publishing, Cham, 2018, https://doi.org/10.1007/978-3-319-73999-1.
[33] M. Lufaso, ch5_solid_state.pdf, chapter 5 solid state. (n.d.). https://www.unf.edu/~michael.lufaso/chem4627/ch5_solid_state.pdf (accessed June 19, 2021).
[34] D. Schmool, Solid State Physics, Mercury Learning & Information, Bloomfield, United States, 2016. http://ebookcentral.proquest.com/lib/rowan/detail.action?docID=4895124. (Accessed 27 April 2021).
[35] J.A. Thornton, Structure-zone models of thin films, in: Modeling of Optical Thin Films, International Society for Optics and Photonics, 1988, pp. 95–105, https://doi.org/10.1117/12.941846.
[36] S. Mukherjee, D. Gall, Structure zone model for extreme shadowing conditions, Thin Solid Films 527 (2013) 158–163, https://doi.org/10.1016/j.tsf.2012.11.007.
[37] R.D. Gould, S. Kasap, A.K. Ray, Thin films, in: S. Kasap, P. Capper (Eds.), Springer Handbook of Electronic and Photonic Materials, Springer International Publishing, Cham, 2017, p. 1, https://doi.org/10.1007/978-3-319-48933-9_28.
[38] H. Sree, Principles of Vapor Deposition of Thin Films, Elsevier, 2006, https://doi.org/10.1016/B978-0-08-044699-8.X5000-1.
[39] G. Taylor, R. Paladines, A. Marti, D. Jacobs, S. Tint, A. Fones, H. Hamilton, L. Yu, S. Amini, J. Hettinger, Electrochemical enhancement of reactively sputtered rhodium, ruthenium, and iridium oxide thin films for neural modulation, sensing, and recording applications, Electrochim. Acta 394 (2021) 139118, https://doi.org/10.1016/j.electacta.2021.139118.